Industrial Crops & Products 237 (2025) 122284

Contents lists available at ScienceDirect

Industrial Crops & Products

journal homepage: www.elsevier.com/locate/indcrop

Biomass synchronous pyrolysis-activation-ammoniation for N-doped biochar: Relationship among biomass, biochar, and electrochemical performance

Xu Chen [a,1], Xuan Tao [b,1], Yurou Wang [b], Xiaolei Shi [b], Zijun Pan [b], Wei Chen [b,*], Zhen Fang [b]

[a] School of Modern Industry for Selenium Science and Engineering, Wuhan Polytechnic University, Wuhan 430023, China
[b] College of Engineering, Nanjing Agricultural University, 666 Binjiang Avenue, Nanjing 211800, China

ARTICLE INFO

Keywords:
Biomass
Synchronous pyrolysis-activation-ammoniation
Porous N-doped biochar
Electrochemical applications
Relationship

ABSTRACT

Preparing N-doped biochar from biomass pyrolysis is a highly valued utilization direction of biomass resource. Herein, porous N-doped biochar was prepared from ten types of agricultural and forestry residues via synchronous pyrolysis-activation-ammoniation of biomass, and the relationship among feedstock properties, biochar properties, and electrochemical performance was investigated. Results showed that the synergistic effect of ammonia and KOH significantly enhanced both the specific surface area (S_{BET}) and N content of the N-doped biochar, with the S_{BET} of biochar exceeding 799 m^2/g and the N content exceeding 3.44 wt%. Specifically, the N-doped biochar from cotton stalk exhibited the highest S_{BET} of 1470.99 m^2/g and a N content of 8.61 wt%. The porous structure comprised mainly abundant micropores and narrow mesopores, which facilitated electrolyte transport effectively. Electrochemical tests showed that N-doped biochar from cotton stalk achieved a specific capacitance of 212.6 F/g in supercapacitor, maintaining an 84 % capacity retention at 10 A/g. In the oxygen reduction reaction (ORR) evaluation, N-doped biochar from cotton stalk achieved a half-wave potential ($E_{1/2}$) of 0.791 V and a limiting current density (J_L) of 5.77 mA/cm^2, demonstrating excellent energy storage and catalytic performance. Biomass rich in lignin and low in ash yielded N-doped biochar with high S_{BET} and N content, with abundant pyridinic-N, pyrrolic-N, quaternary-N, O-C=O/-OH, and O-C=O/C=O functional groups; these properties of N-doped biochar exhibited excellent electrochemical performance in supercapacitor and ORR catalysis. The results could expand the research boundary for high-value utilization of biomass and the synthesis of multifunctional biochar material.

1. Introduction

In order to promote sustainable development and achieve carbon neutrality, the accelerated deployment and exploitation of renewable energy resources have become imperative (Culaba et al., 2023). Biomass is a green, renewable resource with huge reserves and a wide variety of types (Tan et al., 2015). Biomass pyrolysis can obtain biochar, bio-oil, and syngas (Liu et al., 2023). Biochar has attracted intense research attention for advanced biochar-materials (Yang et al., 2021). However, biochar from direct pyrolysis cannot satisfy high-performance applications (Zhang et al., 2022). To prepare multifunctional biochar materials with high value, it is crucial to develop abundant porosity surface active sites (Li et al., 2012).

To achieve high-quality porous N-doped biochar, well-optimized activation and tailored chemical modification procedures are essential (Li et al., 2022). Among various activation methods, KOH activation is one of the most widely used due to its superior activation efficiency, lower activation temperature, and the ability to produce biochar materials with high microporosity and S_{BET} (Li et al., 2020). Chen et al. (2020b) revealed that during biomass pyrolysis, KOH can not only react with the carbon skeleton to induce etching but also interacts with O-containing functional groups, generating abundant new pores and introducing additional O-containing functional groups. Besides, extensive research has been conducted on the preparation of N-doped biochar through introducing nitrogen during biomass pyrolysis (Fu et al., 2023; Lian et al., 2016; Ma et al., 2025). The exogenous nitrogen sources

---

* Correspondence to: 666 Binjiang Avenue, Nanjing 210031, China.
E-mail address: chenwei_hk@163.com (W. Chen).
[1] in the author information indicates equal contribution

https://doi.org/10.1016/j.indcrop.2025.122284
Received 1 August 2025; Received in revised form 20 October 2025; Accepted 10 November 2025

Table 1
Characteristics of biomass.

Materials	Elemental composition (wt%,d)					Proximate analysis (wt%,d)		Fiber composition (wt%,d)			
	C	H	N	S	O*	Volatile Matter	Ash	Fixed Carbon*	Cellulose	Hemicellulose	Lignin
Corn straw	38.36	5.86	1.21	0.15	45.16	64.05	9.26	26.69	29.325	16.04	19.45
Peanut straw	48.55	6.21	0.47	0	41.37	80.1	3.4	16.5	35.18	12.31	28.99
Soybean Stalk	44.87	5.855	1.18	0	40.515	66.02	7.58	26.4	28.725	15.77	18.39
Wheat Stalk	36.7	5.7	0.6	0	47.66	74.13	9.34	16.53	36.1	26.1	22.6
Cotton Stalk	43.5	5.9	0.6	0	46.57	80.22	3.43	16.35	32.9	16.4	27.8
Rice Straw	40.59	5.08	0.57	0	37.06	69.61	16.7	13.69	33.925	15.185	21.04
Pine Wood	49.495	5.86	0.03	0	44.505	87.23	0.11	12.66	43.52	18.495	29.27
Moso Bamboo	48.95	5.31	0.34	0	44.53	81.79	0.77	17.44	39.42	22.41	35.38
Birch Wood	48.41	6.06	0.06	0	45.07	85.9	0.4	13.7	37.245	12.945	25.46
Peanut Shell	51.08	6.19	0.98	0	39.07	76.9	2.68	20.42	29.325	13.535	34.91

d : dry basis.*: Content was calculated by difference, O (wt%) = 100 wt%-(C+H+N + S+ Ash). Fixed carbon (wt%) = 100 wt%-Volatile Matter-Ash.

include urea, melamine, ammonium salts, and ammonia (Wan et al., 2020). Ammonia has been proven to be an effective surface modification technique for introducing various nitrogen functional groups (e.g., pyridinic-N, graphitic-N, and -NH_2) onto the surface of biochar (Zhang et al., 2014; Zhu et al., 2018). To further obtain biochar with porous and N-rich properties, integrating activators and nitrogen sources to achieve simultaneous activation and nitrogen doping of biomass has gained widespread attention. We proposed synchronous pyrolysis-activation-ammoniation of biomass, and prepared the N-doped biochar with high porosity and N content in a relative mild condition, based on the synergistic effect of activation and nitrogen doping process (Wang et al., 2024). Nevertheless, preparation mechanism of N-doped biochar still needs to be studied in depth, as well as the method applicability.

Tailoring the hierarchical pore architecture and interfacial chemistry of N-doped biochar enables improvements in electrochemical adsorption capability and ion transport kinetics; consequently, porous N-doped biochar holds great promise in fields of supercapacitors, and ORR catalysis (Oladunni et al., 2018). The S_{BET}, pore size, and elemental composition of biochar materials are important factors affecting the specific capacitance and electrochemical properties of biochar electrodes (de Almeida et al., 2020), while the characteristics of biomass derived biochar are predominantly dictated by feedstock and pyrolysis conditions (Rajapaksha et al., 2016). Thus, clarifying the structure-property relationship between biomass feedstock characteristics, biochar properties, and electrochemical performance is essential. Nzediegwu et al. (2021) revealed that variations in cellulose and lignin N content among the biomass led to distinct differences in the S_{BET} and pore size distribution of the derived biochar. Arkhipova et al. (2022) and Zhang et al. (2023) found a well-developed pore structure of biochar (>2000 m^2/g) demonstrated excellent electrochemical properties and recycling stability. Yet, no systematic study has linked biomass properties to both the structure of N-doped biochar and its electrochemical behavior.

In this study, the universality of synchronous pyrolysis-activation-ammoniation of biomass for porous N-doped biochar was investigated, using ten types of agricultural and forestry biomass. And further analyses systematically summarized how biomass composition shaped the properties of N-doped biochar and, in turn, dictated its electrochemical performance. Findings could provide theoretical insights and practical guidelines for the valuable utilization of biomass, eco-friendly synthesis of N-doped biochar, and its multifunctional application.

2. Materials and methods

2.1. Materials

Ten types of agricultural and forestry biomass, including wheat straw and peanut shells (collected from Huanghai Farm, yancheng, Jiangsu), cotton stalk (Shawan County, Xinjiang), bamboo (Wuhu, Anhui), and soybean straw, rice straw, corn straw, peanut straw, pinewood, and birch (Jiangsu), were ground and sieved to ensure particles with a size range of 40–80 mesh. To remove moisture, all biomass samples were dried at 105 °C for 1 day.

The proximate analysis of the biomass was performed by the Chinese national standard GB/T 28731–2012. Cellulose, hemicellulose, and lignin contents were quantified with an ANKOM 2000 fiber analyzer (ANKOM Technology, Macedon, NY). (Larter, 1992). A CHNS/O elemental analyzer was employed to perform the elemental composition determination (Vario Micro Cube, Elementar, Germany), and the results are placed in Table 1.

Biomass was pretreated via an impregnation method. Considering the pore-forming efficiency and economic feasibility, each biomass sample (3 g) was mixed with potassium hydroxide (1.5 g) at a mass ratio of 2:1, and 30 mL of deionized water was added to ensure uniform dispersion under continuous stirring.

2.2. Experiments

All experiment runs were carried out in a bench-scale tubular fixed-bed unit (45 mm in internal diameter and 600 mm in height), a feeding device, a liquid nitrogen condenser, an ice-water mixture trap, a drying bottle, a gas-flow regulator, and thermal-control module. The schematic diagram was shown in our previous research (Chen et al., 2020a).

Prior to the experimental run, the biomass-loaded quartz basket was positioned at the reactor's uppermost section, and high-purity argon (Ar, 99.9 %) flowed through the reactor at 200 mL/min to ensure complete purging residual air. Once the air was completely displaced, the Ar flow rate was reduced, and a gas mixture of 50 vol% ammonia (NH_3, 99.9 %) was introduced. The total flow rate of Ar and NH_3 was maintained at 200 mL/min. Upon region for reaction attaining 600 °C, the quartz basket was swiftly translocated to the isothermal reaction zone, and the temperature was maintained at the target temperature for 30 min. After the reaction, NH_3 flow was stopped during the cooling process, and then reactor was subsequently quenched to ambient temperature under a continuous Ar flow.

The resulting biochar products were washed with acid, filtered, and dried to obtain porous N-doped biochar. The samples prepared from different biomass were designated as follows: corn straw biochar (CSWB), pinewood biochar (PWB), soybean straw biochar (SSB), wheat straw biochar (WSB), cotton stalk biochar (CSKB), rice straw biochar (RSB), bamboo biochar (BBB), birch biochar (BIB), peanut shell biochar (PSLB), and peanut straw biochar (PSWB).

2.3. Characterization

2.3.1. Structure characterization

Elemental composition of the porous N-doped biochar was established via CHNS/O analyzer (Thermo Flash 2000, USA). Surface chemical functional functional groups were characterized by XPS using a

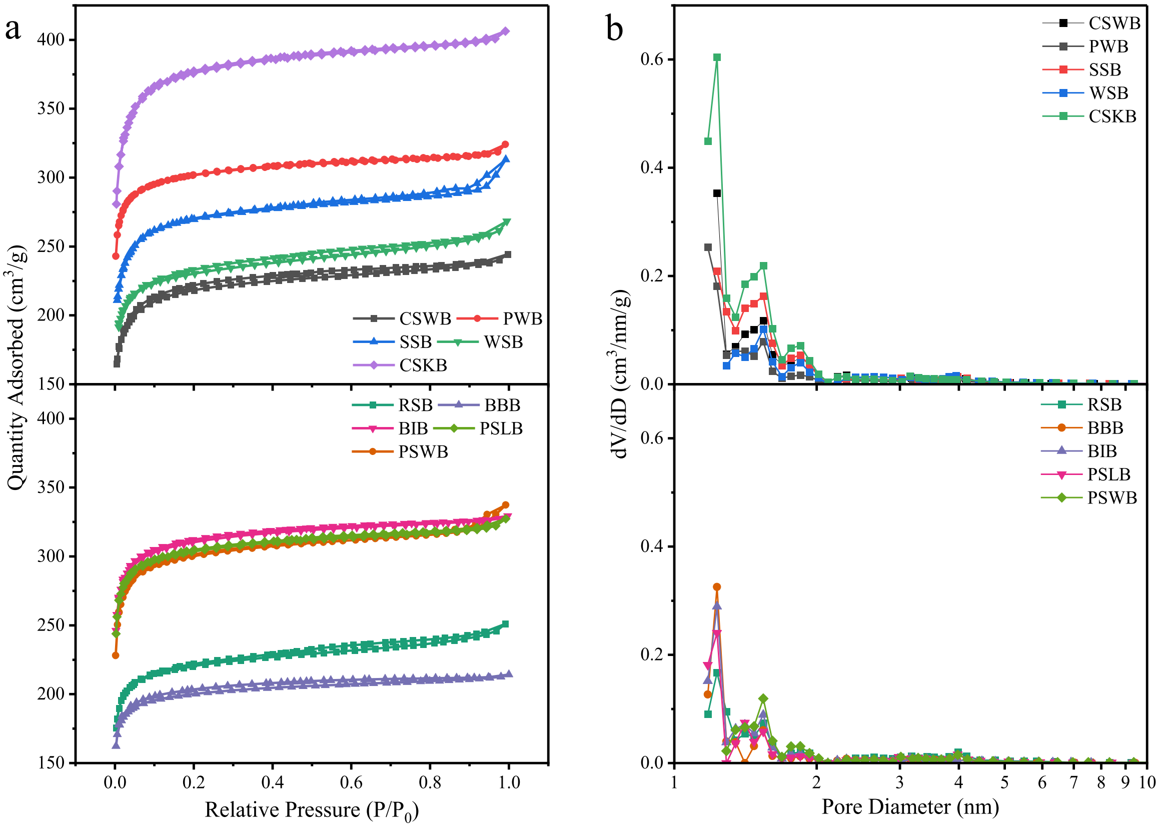

Fig. 1. (a) N_2 adsorption-desorption isotherms and (b) pore size distribution of porous N-doped biochar.

Thermo Scientific K-Alpha spectrometer (USA). The pore architecture of the biochar was assessed by N_2 adsorption-desorption isotherms at 77 K on an ASAP analyzer (NOVA 4200e, Quantachrome Instruments, USA). Before analysis, samples were degassed at 150 °C lasting for at least 10 h, and the specific surface area (S_{BET}) was subsequently calculated from BET measurements. Pore-size distributions were derived from DFT calculations, whereas micropore volumes were quantified via t-plot analysis. XRD (Bruker D8 Advance, Germany) was performed to probe the crystal structure of the washed biochar. Raman spectroscopy (Horiba LabRAM HR Evolution, Japan) was employed to analyze the graphitization degree and defect structure of the samples.

2.3.2. Supercapacitor performance valuation

Ni foam was used as the current collector and cut into rectangular pieces with dimensions of 1 × 2 cm^2. The cut nickel foam was sequentially immersed and ultrasonically treated for 30 min in 1 mol/L dilute hydrochloric acid, deionized water, and absolute ethanol to remove surface impurities. After cleaning, The Ni foam underwent vacuum drying at 60 °C for 6 h. The mass of treated Ni foam was measured and recorded as m_1.

To fabricate the working electrode, porous N-doped biochar, acetylene black, and PTFE were blended at an 8:1:1 mass ratio within a sample vial. Then, absolute ethanol (500 μL) served as the solvent, followed by 2 h of sonication to achieve a uniform dispersion. The obtained slurry was pipetted onto pre-treated Ni foam to coat a 1 × 1 cm^2. The electrode was then vacuum-dried at 80 °C for 12 h, followed by compression at 12 MPa for 5 min in a tablet press to improve adhesion and lower interfacial resistance. The mass of the prepared electrode was measured and recorded as m_2. The mass of the loaded porous N-doped biochar was calculated according to $(m_2\text{-}m_1) \times 0.8$, and the final loading amount was controlled within the range of 1.5–2.5 mg.

Electrochemical tests were run in a three-electrode cell on a CHI660E workstation (CH Instruments, China): the as-prepared biochar electrode served as the working electrode, a 1 × 1 cm^2 Pt foil as the counter electrode, and a saturated Hg/HgO electrode (with a 1.0 mol/L KOH salt bridge) served as the reference. The tests were conducted in 6 M KOH at 25 °C.

Cyclic voltammetry (CV) was employed to analyze the relationship between electrode potential and current response. The CV curves were used to identify the capacitive behavior and determine the contribution types of the electrodes. The tests were carried out in a voltage window.

Galvanostatic charge-discharge (GCD) measurements were conducted within a specific potential window at constant current densities to obtain the relationship between potential and time. The GCD curves were used to derive the electrodes' specific capacitance and rate capability. When the GCD curve exhibited an ideal isosceles triangular shape, the specific capacitance of the biochar material was calculated using Eq. (1). In cases where the GCD curve displayed deviations from the ideal triangular shape due to pseudocapacitive contributions, Eq. (2) was applied for capacitance calculation.

$$C_m = (I \times \Delta t)/(m \times \Delta V) \tag{1}$$

$$C_m = \left(2I\int V dt\right) \Big/ \left(m \times (V_2{}^2 - V_1{}^2)\right) \tag{2}$$

Where C_m is specific capacitance of the electrode material (F/g), I is the discharge current (A), Δt is the discharge time (s), m is the mass of the porous N-doped biochar material loaded on the working electrode (g), and ΔV is the potential change during the discharge process (V).

Electrochemical impedance spectroscopy (EIS) was performed to investigate the electrochemical properties of the materials by measuring the impedance over a wide frequency range. Electrochemical impedance spectra were collected at the open-circuit potential from 0.01 Hz to 100 kHz under a 5 mV AC perturbation. The impedance data were fitted using ZView software, and the Nyquist plots were generated based on the measured results.

2.3.3. ORR electrocatalytic performance valuation

For catalyst ink preparation, 5 mg of the sample and 1 mg of acetylene black were uniformly dispersed in 10 μL of Nafion solution and 490 μL of absolute ethanol. The mixture was sealed and subjected to ultrasonic treatment for 2 h to obtain a homogeneous catalyst ink.

The glassy carbon electrode (GCE) was polished on a felt pad using alumina powders with different particle sizes to achieve a smooth surface. The polished electrode was then cleaned by sequential ultrasonic treatment in deionized water and absolute ethanol for 2–3 min to remove surface residues. After drying, 10 μL of the uniformly dispersed catalyst ink was drop-cast onto the GCE surface using a micropipette and allowed to dry naturally in air. The prepared electrode was subsequently assembled onto a rotating disk electrode (RDE) system for electrochemical performance evaluation.

ORR activity was evaluated in 0.1 M KOH within a three-electrode cell employing a saturated calomel reference (SCE, saturated KCl); all potentials were converted to the RHE scale through Eq. (3). A graphite rod functioned as the auxiliary electrode. Before the measurements, O_2 was purged into the electrolyte for at least 30 min to ensure oxygen saturation. During the ORR tests, oxygen flow was continuously maintained throughout the entire measurement process to prevent oxygen depletion.

$$E(\mathrm{RHE}) = E(\mathrm{SCE}) + 0.0592 \times \mathrm{pH} + 0.241 \quad (3)$$

CV test was first swept between −1.0 and 0.2 V at 10 mV/s under static conditions to capture ORR voltammograms; subsequently, non-Faradaic scans from −0.05–0 V were recorded at 2–10 mV/s to extract the double-layer capacitance.

Linear sweep voltammetry (LSV) was executed over −1.0–0.2 V at 10 mV/s. The rotation speeds of the RDE were set to 1600, 1225, 900, 625, and 400 rpm to obtain the LSV curves. From the LSV data, the limiting current density, Tafel slope, half-wave potential ($E_{1/2}$), and onset potential (E_{onset}) were calculated. Furthermore, the electron-transfer count for ORR was extracted from LSV data via the Koutecky-Levich (K-L) relations given in Eqs. (4) and (5).

$$1/J = 1/J_L + 1/J_k = 1\Big/\left(B\omega^{\frac{1}{2}}\right) + 1/J_k \quad (4)$$

$$B = 0.2nFC_0D^{2/3}v^{-1/6} \quad (5)$$

Here, J denotes the experimental current density (mA/cm^2), J_L the diffusion-limited current density (mA/cm^2), and J_k the kinetic current density (mA/cm^2). Angular velocity ω (rpm) relates to rotation rate, F =96485 C/mol is the Faraday constant, $C_0 = 1.2 \times 10^{-6}$ mol/L is the dissolved O_2 concentration, $D = 1.9 \times 10^{-5}$ cm^2/s is diffusion coefficient, and $\nu = 0.01$ cm^2/s is the kinematic viscosity of 0.1 M KOH.

EIS was carried out at the open-circuit potential from 1 Hz to 100 kHz with a 5 mV perturbation, fitted in ZView, and plotted as Nyquist diagrams.

3. Results and discussion

3.1. Structure characterization of N-doped biochar

Fig. 1(a) illustrates the pore structure of the porous N-doped biochar. The samples such as CSKB, PWB, BIB, PSLB and PSWB exhibited typical Type I isotherms, indicative of predominantly microporous structures. While the curves of some materials exhibited a combination of Type I and Type IV characteristics, such as SSB, WSB, CSWB, BBB and RSB, indicative of the material featuring a microporous-mesoporous multilevel pore structure. Nitrogen uptake rose steeply once the relative pressure dropped below 0.1, reflecting micropore filling; Between $P/P_0 = 0.1$ and 0.3, a gradual increase in adsorption capacity was found, reaching equilibrium with the further increase in pressure. This behavior suggests the presence of mesopores within the N-doped biochar. The mesopores are beneficial for improving ion diffusion pathways and reducing mass transfer resistance, which is particularly advantageous for subsequent electrochemical energy storage applications (Rufford et al., 2009). When P/P_0 exceeded 0.9, the adsorption capacity showed another significant increase. This phenomenon was typically associated with the formation of macropores or interparticle voids, which may result from the partial exfoliation of layered structures during high-temperature activation. The hierarchical pore structure, integrating micropores, mesopores, and macropores, facilitated the synergistic optimization of S_{BET} and ion transport efficiency.

Table 2
N_2 adsorption-desorption analysis results of porous N-doped biochar.

Samples	S_{BET} (m^2/g)	V_{total} (cm^3/g)	V_{micro} (cm^3/g)	$V_{meso+macro}$ (cm^3/g)	V_{micro}/V_{total}
CSWB	848.03	0.378	0.274	0.104	0.725
PSWB	1196.53	0.522	0.403	0.119	0.772
SSB	1052.93	0.484	0.352	0.132	0.727
WSB	907.55	0.415	0.297	0.118	0.715
CSKB	1470.99	0.629	0.493	0.136	0.784
RSB	872.44	0.388	0.290	0.098	0.747
PWB	1207.78	0.501	0.412	0.089	0.822
BBB	799.21	0.332	0.272	0.060	0.851
BIB	1237.4	0.545	0.416	0.129	0.763
PSLB	1213.8	0.506	0.419	0.087	0.827

$V_{meso+macro}$: Mesopore and macropore volume, $V_{meso+macro} = V_{total} - V_{micro}$.

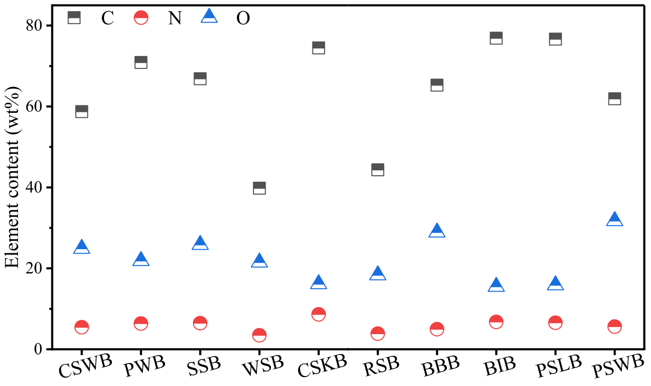

Fig. 2. Elemental composition of the porous N-doped biochar.

According to the pore size distribution curves (Fig. 1(b)), the biochar exhibited a hierarchical pore architecture dominated by micropores and narrow mesopores (2–5 nm), which were consistent with the aforementioned isotherm analysis. As shown in Table 2, CSKB exhibited the highest S_{BET} and total pore volume (V_{total}), reaching 1470.99 m^2/g and 0.629 cm^3/g, respectively. By comparison, BBB exhibited the lowest S_{BET} and V_{total} values (799.21 m^2/g and 0.332 cm^3/g). Most of the biochar exhibited a micropore volume ratio ($V_{micro}/V_{total)}$ between 0.7 and 0.8.

Elemental analysis of the porous N-doped biochar is shown in Fig. 2. The carbon content was within the range of 60–80 wt%, while the oxygen content ranged from 15 to 25 wt%. CSKB, BIB, and PSLB exhibited relatively higher carbon content, which may be closely related to the inherent higher proportions of cellulose and lignin (Sun et al., 2017). In contrast, WSB and RSB displayed significantly lower carbon content of 39.81 wt% and 44.34 wt%, respectively. The carbon content of WSB and RSB became comparable to those of the other biochar by normalization after ash content removal, indicating that the low apparent carbon content was primarily due to the biomass’s elevated ash level rather than differences in activation or pyrolysis process.

CSKB exhibited the highest N content, reaching 8.61 wt%. The N contents of the other biochar mainly ranged from 3.85 wt% to 6.75 wt

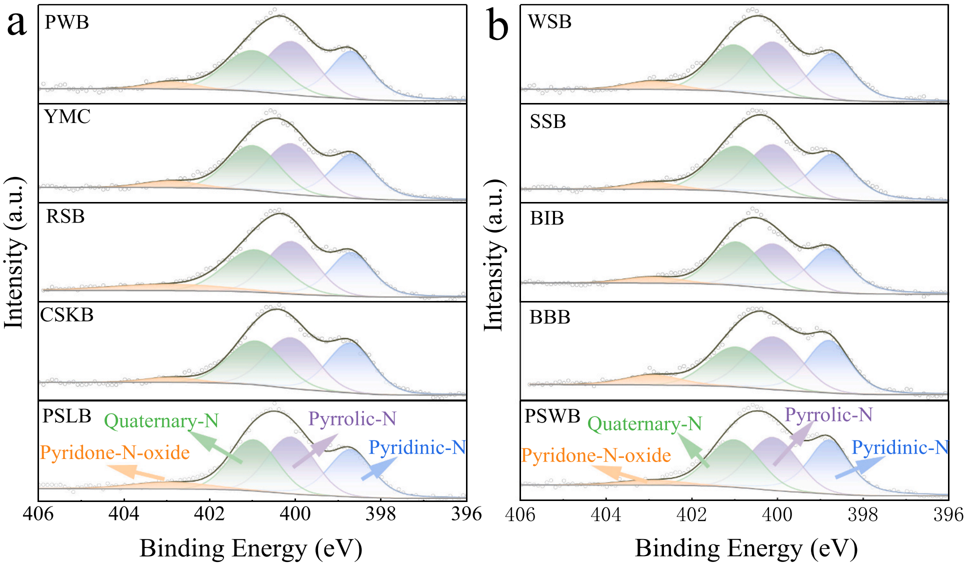

Fig. 3. The N1s peak plots of porous N-doped biochar.

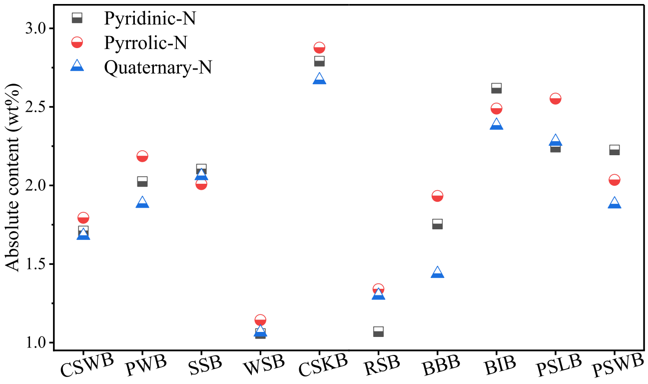

Fig. 4. Absolute content of pyridinic-N, pyrrolic-N, and quaternary-N in the porous N-doped biochar.

%. After ash-free normalization, the N contents of WSB and RSB also fell within this range. These results demonstrated that synchronous pyrolysis-activation-ammoniation of biomass for porous N-doped biochar achieved efficient nitrogen incorporation across various biomass sources, exhibiting good universality. Under the activation effect of KOH, O-containing functional groups in biomass are etched, creating defects and vacancies in the carbon skeleton. Subsequently, NH_3 and its radicals (NH_2*, NH*) diffused into these active sites and bonded with the carbon skeleton, forming stable N-containing functional groups (Chen et al., 2020b; Zhang et al., 2016). This process effectively increased the N content on the biochar surface, providing abundant active sites for subsequent applications in electrochemical energy storage and catalysis.

Fig. 3 presents the N1s spectra of the N-doped biochar. The N-containing functional groups are primarily composed of pyridine-N-oxide (402.9–403.5 eV), quaternary-N (400.9–401.5 eV), pyrrolic-N (399.5–400.1 eV), and pyridinic-N (398.2–398.8 eV) (Chen et al., 2020a). Pyridinic-N and pyrrolic-N were the dominant N-containing functional groups at 600 °C, usually accounting for more than 60 % of

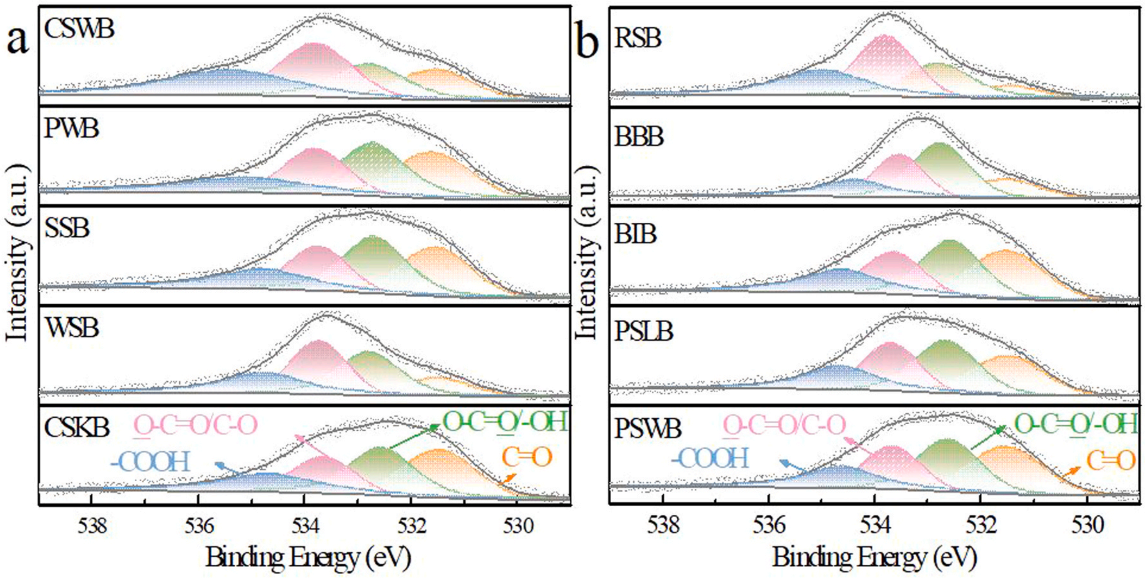

Fig. 5. The O1s peak plots of porous N-doped biochar.

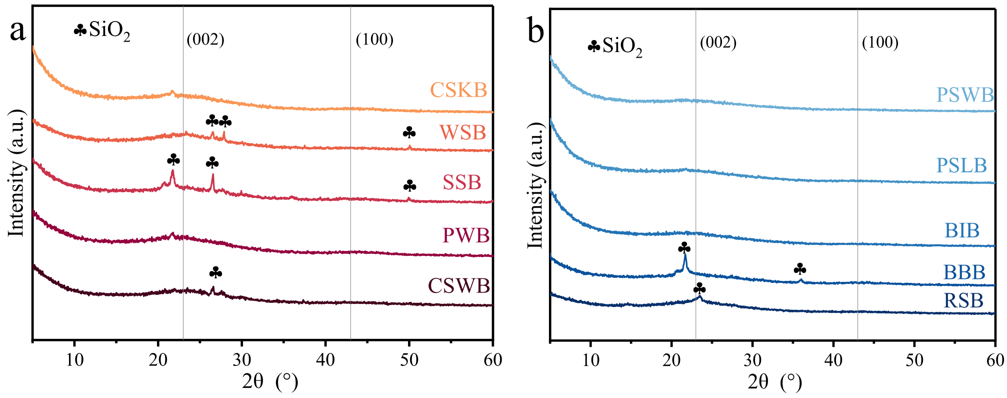

Fig. 6. The patterns of porous N-doped biochar.

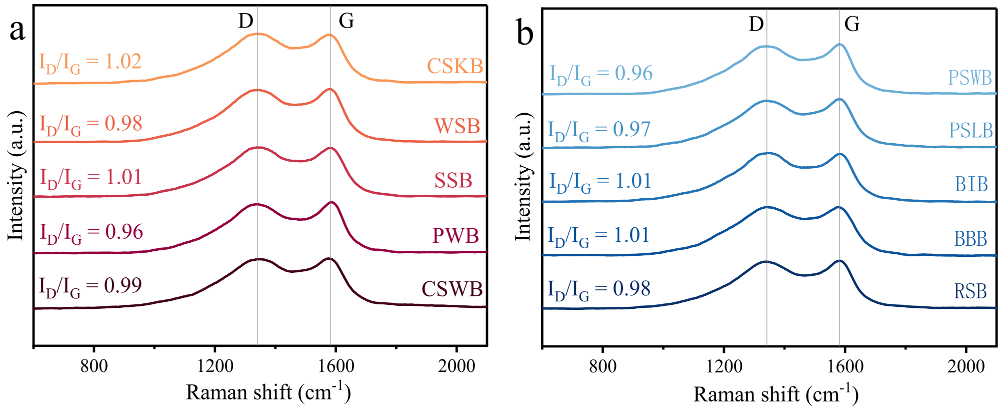

Fig. 7. Raman spectroscopy of porous N-doped biochar.

the total N content (Chen et al., 2017).

Based on the N content and the relative proportions of N, the absolute yield of pyridinic-N, pyrrolic-N, and quaternary-N was calculated, as shown in Fig. 4. CSKB exhibited the highest content of all three N-containing functional groups. The abundant pyrrolic-N and quaternary-N in CSKB could enhance O_2 adsorption, improve electronic conductivity, and reinforce structural stability, thus boosting ORR activity. Furthermore, the high pyridinic-N content facilitates the coupling of oxygen atoms with protons, promoting electron transfer and accelerating the ORR kinetics (Sun et al., 2018).

The O1s spectra of N-doped biochar are displayed in Fig. 5. O-containing functional groups were identified as carboxyl -COOH (534.3–535.4 eV), O-C=O/C-O (533.1–533.8 eV), O-C=O/-OH (532.3–532.8 eV), and C=O (531.0–531.9 eV) (Chen et al., 2018). O-C=O/C-O and O-C=O/-OH were the abundant O-containing functional groups in all samples, while PWB, SSB, BIB, PSLB, PSWB, and CSKB also exhibited high content of C=O, and the content of -COOH was the lowest in all samples. These O-containing functional groups are beneficial for enhancing the wettability of the biochar material surfaces, thereby enhancing electrolyte-electrode interfacial contact, improving the overall electrochemical performance of the biochar (Wei et al., 2016).

Fig. 6 presents the crystal features of the N-doped porous biochar. Every sample shows broad, low-intensity reflections at near 23°and 44°, indexing to the (002) and (100) planes of graphitic carbon, respectively (Yan et al., 2017). The broad (002) peak at around 23° indicates a predominantly amorphous carbon structure with disordered layer stacking, while the (100) peak at approximately 44° reflects in-plane structural disorder of carbon atoms (Chen et al., 2024). These results confirmed that the porous N-doped biochar exhibited low graphitization degrees and was mainly amorphous. Synchronous pyrolysis-activation-ammoniation of biomass not only facilitated the formation of hierarchical pore structures but also introduced abundant defects and edge sites into the carbon layers. This process inhibited the orderly growth of graphitic domains, resulting in reduced graphitization (Yan et al., 2017).

In addition, several sharp diffraction peaks were observed in the patterns of some samples, mainly at 21.7°, 23.6°, 26.5°, 27.6°, 36°, and 49.7°, which correspond to the (92), (198), (180), (154), (152), and (210) planes of SiO_2, respectively. This indicated that a considerable amount of silica remains in CSWB, SSB, WSB, RSB, and BBB. SiO_2 could not be effectively removed during the acid washing process, resulting in its retention in the final biochar.

Raman spectroscopy the porous N-doped biochar is shown in Fig. 7. All samples exhibited I_D/I_G ratios close to 1, indicating that the biochar a reasonable combination of order and defects. CSKB displayed the highest I_D/I_G ratio, which could be attributed to its higher N content and more developed porous structure. This result was consistent with the elemental and pore structure results, further underscoring how concurrent N incorporation and pore engineering jointly amplify defect formation in the biochar.

To investigate the influence of biomass properties on the S_{BET} and N content of the porous N-doped biochar, the relationships among S_{BET}, N content, proximate analysis, and biomass composition are presented in Fig. 8. As shown in Fig. 8(a), the S_{BET} of N-doped carbon (from 848.03 to 1471.99 cm^2/g) was positively correlated with lignin content (from 19.45 to 27.8 wt%) and slightly negatively correlated with hemicellulose content (from 16.61 to 16.4 wt%), while cellulose seemed not to

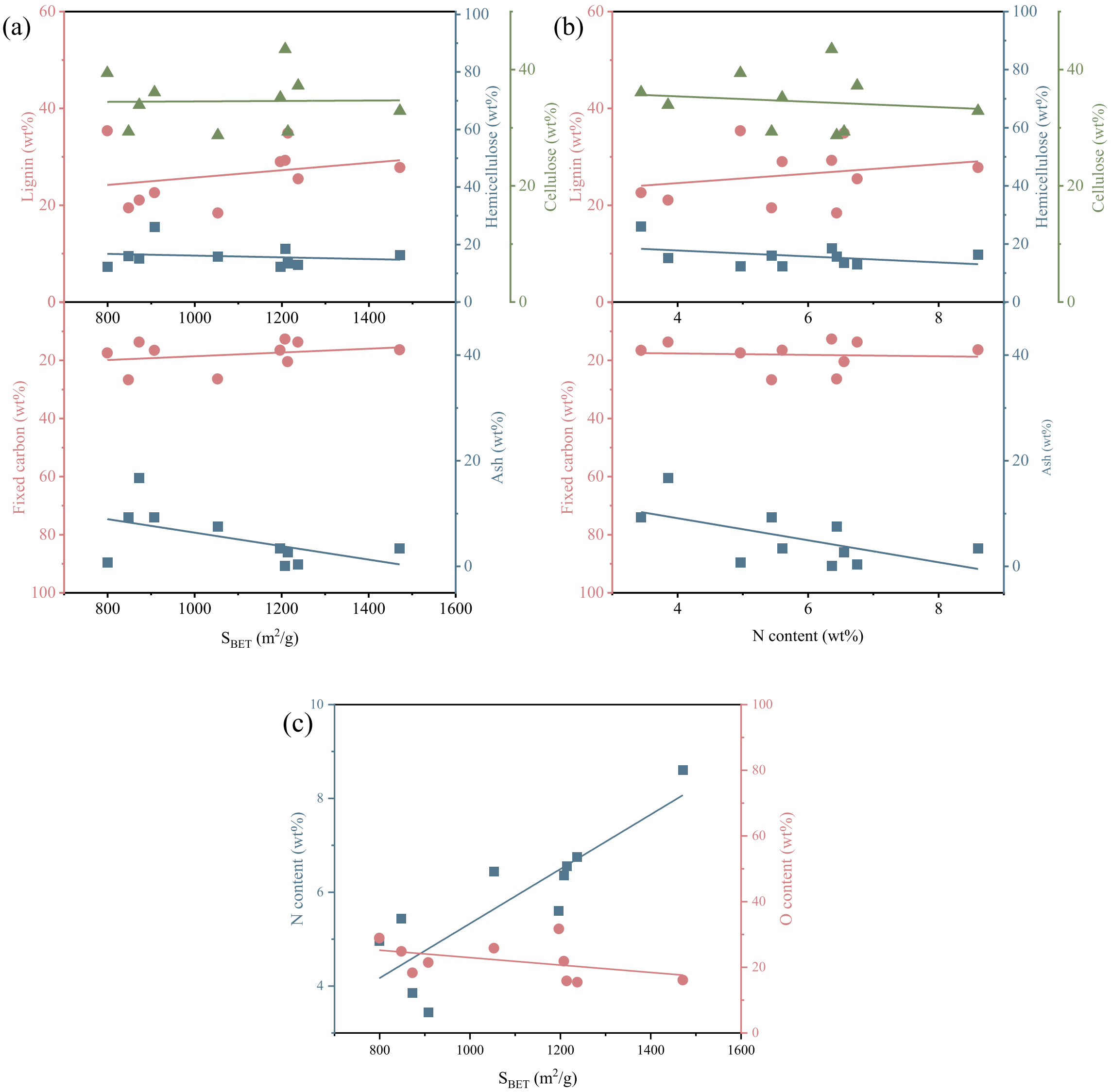

Fig. 8. Relationships between biochar properties and biomass characteristics.

show direct effect on S_{BET}. As to proximate analysis, S_{BET} of N-doped carbon was both negatively correlated with ash content (from 9.26 to 3.43 wt%) and fixed carbon content (from 17.44 to 16.35 wt%). Large amounts of hemicellulose were converted into highly mixed non-condensable gases, which was not major contributor to carbon yield. The result was consistent with findings from previous studies that removal of hemicellulose helps increase the S_{BET} and pore volume of biochar (He et al., 2023). Lignin, due to its high fixed carbon content, contributes to a high carbon yield; simultaneously, an appropriate amount of cellulose can inhibit lignin decomposition, thereby producing more solid carbon (Zhao et al., 2023). Biomass with high ash content left much ash residue in biochar after pyrolysis, blocking microporous channels (Grafmüller et al., 2022), thereby reducing S_{BET}. Fig. 8(b) shows that N content (from 3.44 to 8.61 wt%) also exhibited an intensively positive correlation with lignin content (from 22.6 to 27.8 wt%), while both cellulose and hemicellulose showed a little negative correlation (from 36.1 to 32.9 wt% and from 26.1 to 16.4 wt%, respectively). Moreover, ash content (from 9.34 to 3.43 wt%) displayed a strong negative correlation while fixed carbon content didn't show apparent correlation. This demonstrates the critical role of biochar yield and pore structure in element loading. As to distinct N-doping configurations, the three primary nitrogen configurations (pyridinic-N, pyrrolic-N and quaternary-N) showed nearly consistent correlations with raw material properties: lignin content exhibited a positive correlation, cellulose content showed a slight negative correlation, while hemicellulose content demonstrated a significant negative correlation with ash content, as illustrated in Fig. S1. Fig. 8(c) illustrated the correlation among S_{BET}, N and O content of N-doped biochar properties. The increase in S_{BET} was accompanied by a decrease in O content and increase in N content, this further proved the reactions between ammonia and oxygen-containing functional groups, indicating that developed pores enhanced the function as element carrier. These findings indicate that synchronous pyrolysis-activation-ammoniation of biomass can universally convert various biomass into porous biochar with high-porosity (799.21–1479.99 cm^2/g), and high N content (3.44–8.61 wt%); low-ash biomass is more likely to obtain porous N-doped biochar.

3.2. Supercapacitor performance

Electrochemical evaluation of the porous N-doped biochar was conducted via CV tests in a three-electrode configuration, shown as Fig. 9. At 10 mV/s, every voltammogram remained almost perfectly

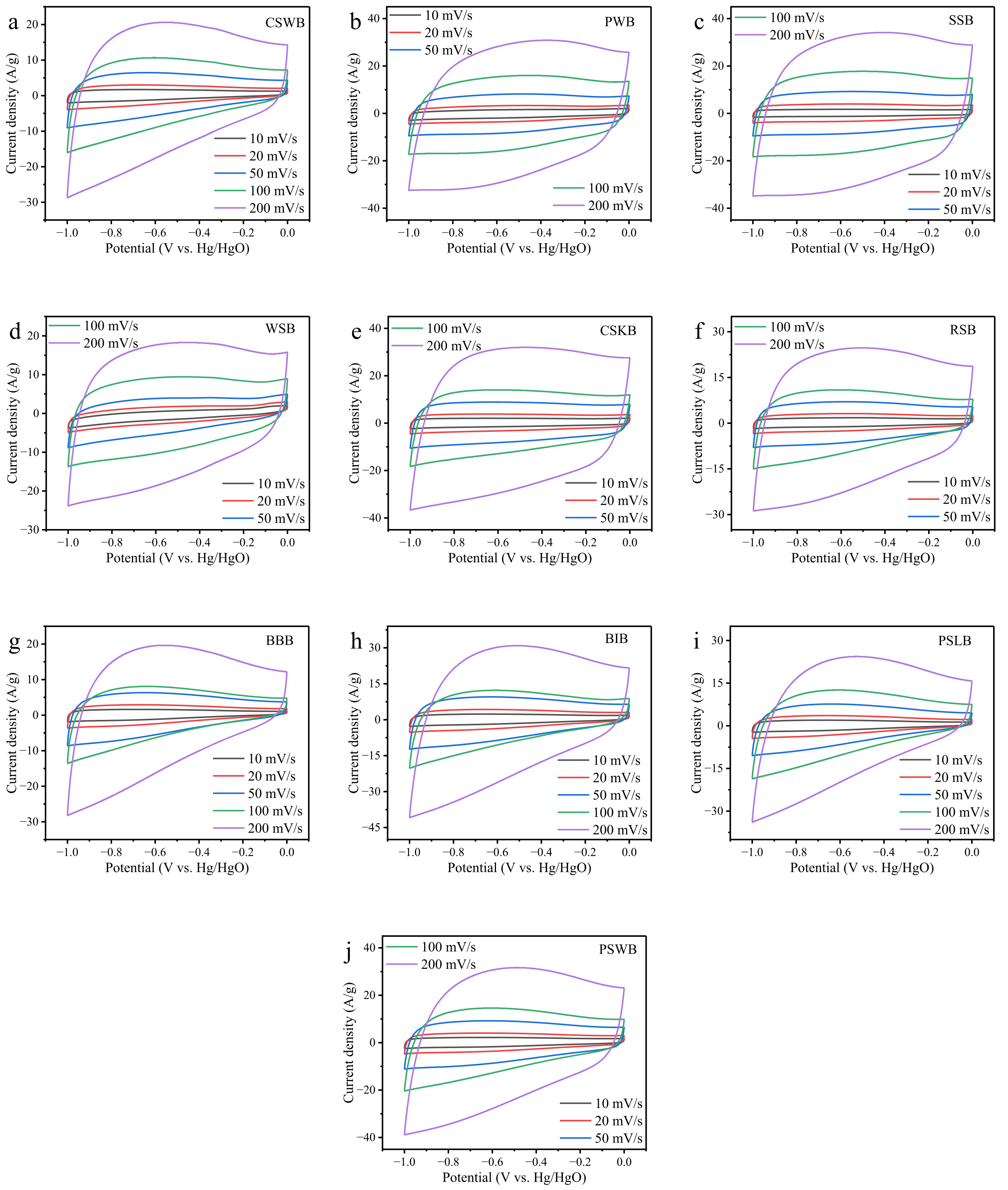

Fig. 9. The CV curves of porous N-doped biochar.

rectangular, evidencing superior electric double-layer capacitive response. The maintenance of this rectangular shape at low scan rates also demonstrated good rate capability, primarily attributed to the synergistic effect of micropores and mesopores. At scan rates above 100 mV/s, the CV profiles of all samples gradually deviated from the ideal rectangular shape. This phenomenon was mainly attributed to redox reactions involving oxygen- and N-containing functional groups, which contribute to pseudo-capacitance (Duan et al., 2019). Pyridinic-N and graphitic-N can facilitate electron transfer processes, while carboxyl and hydroxyl functional groups are prone to reversible redox reactions at higher potentials, jointly enhancing the pseudo-capacitive behavior.

The GCD curves are shown in Fig. 10(a-j). All biochar exhibited

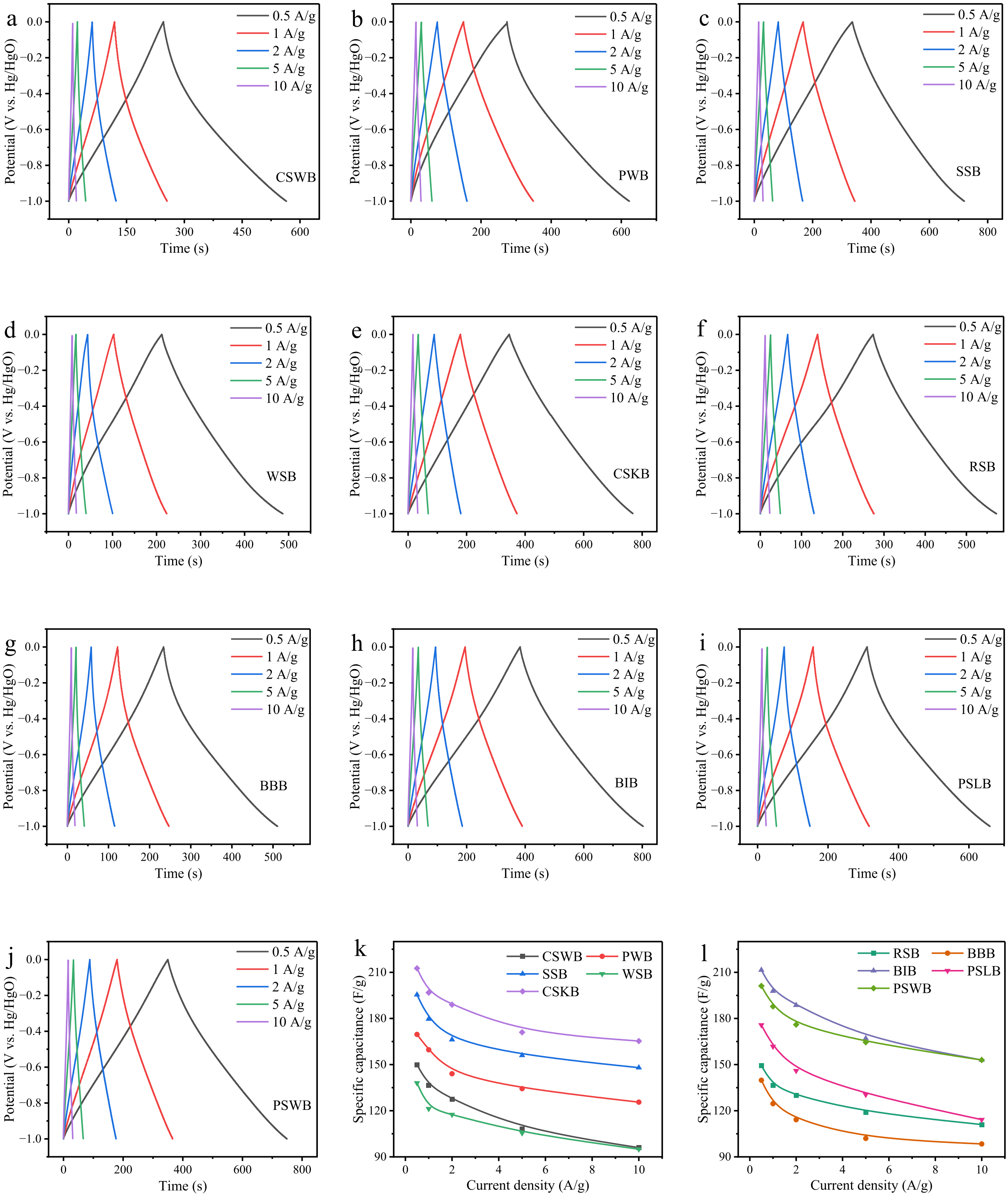

Fig. 10. GCD curves (a–j) and rate performance (k, l) of the porous N-doped biochar.

nearly symmetrical triangular GCD profiles with slight distortions, indicating good reversibility of the charge storage process. Minor deviations from the ideal triangle indicated both electric double layer and faradaic charge storage, in line with the cyclic voltammetry data. Moreover, the absence of significant IR drops in the discharge curves implies low internal resistance and efficient charge transport during the electrochemical process. At a current density of 0.5 A/g, the specific capacitances of CSWB reached 211.50 F/g. This effect likely stemmed from the synergistic impact of abundant nitrogen and an extensive pore network (Liu et al., 2024).

The rate performance of the porous N-doped biochar is illustrated in Fig. 10(k) and (l). With increasing current density, all samples exhibited

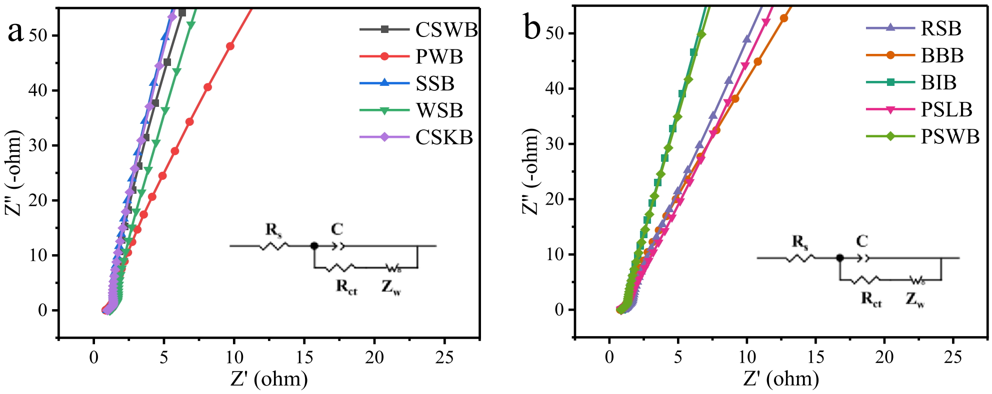

Fig. 11. The Nyquist plots of porous N-doped biochar (Illustration: Equivalent circuit diagram).

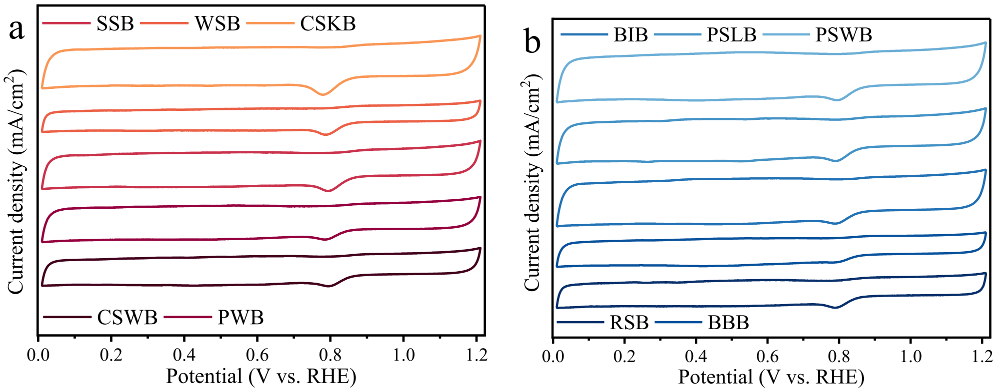

Fig. 12. The CV curves of porous N-doped biochar.

a progressive decline in specific capacitance. This reduction was primarily attributed to the shortened charge-discharge time at higher current loads, which restricted the full utilization of electroactive sites. In addition, higher ion transport resistance within the porous network further limited capacitance retention under fast charging/discharging conditions. At the elevated current density of 10 A/g, RSB delivered the highest specific capacitance (165.3 F/g) and retention (84 %), while all other samples maintained $\geq$ 111 F/g and 70.4 %, respectively. These features collectively ensured outstanding capacitance retention and electrochemical reversibility, even at high current densities.

The Nyquist plots are presented in Fig. 11. Based on the plots, the CSKB demonstrated superior conductivity compared to the other samples. By fitting the EIS data with an equivalent circuit model using ZView software (as illustrated in the figure), the R_{ct} and R_s values for each sample were obtained. Among all the samples, CSKB exhibited the lowest R_{ct} (0.79 Ω) and R_s (0.006 Ω) values, indicating the fastest charge and ion transport ability. The other samples all had R_s values below 1.2 Ω and R_{ct} values below 0.08 Ω, indicating that N doping and the microporous structure effectively suppressed the system resistance.

3.3. ORR electrocatalytic performance

Fig. 12 displays the cyclic voltammograms recorded at 10 mV/s. All samples exhibited distinct oxygen reduction peaks, confirming their catalytic activity toward ORR. CSKB exhibited the highest oxygen-reduction peak potential (E_p). A more positive E_p typically indicated enhanced electrocatalytic activity and lower overpotential for the ORR. Higher N content and abundant structural defects facilitated oxygen molecule adsorption and promoted efficient electron transfer, both of which are essential for accelerating the ORR process.

Rotating-disk LSV (400–1600 rpm) probed the ORR kinetics of the porous N-doped biochar (Fig. 13), obtaining E_{onset}, $E_{1/2}$, and J_L; of these, $E_{1/2}$ is regarded as the prime indicator of activity, as it reflects the potential at which the reaction reaches half of the limiting current; a more positivquane $E_{1/2}$ indicates better catalytic performance. Under 1600 rpm rotation, the $E_{1/2}$ and J_L values of all samples are summarized in Fig. 14. CSKB exhibited the most favorable ORR performance, with an $E_{1/2}$ of 0.791 V and a J_L of 5.77 mA/cm^2, higher than those of the other nine types of biochar ($E_{1/2} = 0.754$–0.789 V; $J_L = 4.37$–5.58 mA/cm^2). CSKB also registered the highest onset potential of the series, underscoring its superior ORR performance. This enhanced performance is likely due to its high absolute yield of pyridinic-N and quaternary-N functional groups. Pyridinic-N is known to improve E_{onset} by facilitating initial O_2 adsorption and electron transfer (Zhang et al., 2021), while quaternary-N can contribute to higher limiting current densities by enhancing electron conductivity and catalytic site availability (Ding et al., 2022). K-L plots were also constructed at a potential of 0.2 V. Linearity of the plots indicated that oxygen reduction in these samples follows first-order kinetics for dissolved O_2 concentration. K-L plots revealed electron-transfer numbers near four, indicating a predominantly four-electron ORR mechanisms. These mechanisms directly reduced O_2 to OH^-, improving reaction kinetics, enhancing faradaic efficiency, and minimizing the formation of undesirable peroxide intermediates.

Further analysis of LSV data were re-plotted as Tafel curves (Fig. 15 (a) and (b)) via linear fitting; the resulting slope gauges ORR kinetics, with smaller values signifying faster charge-transfer and more rapid approach to the limiting current density (J_L) (Song et al., 2019). WSB exhibited the smallest Tafel slope (91.8 mV/dec), benefiting from the promotion of surface adsorption and electron pathways by residual SiO_2;

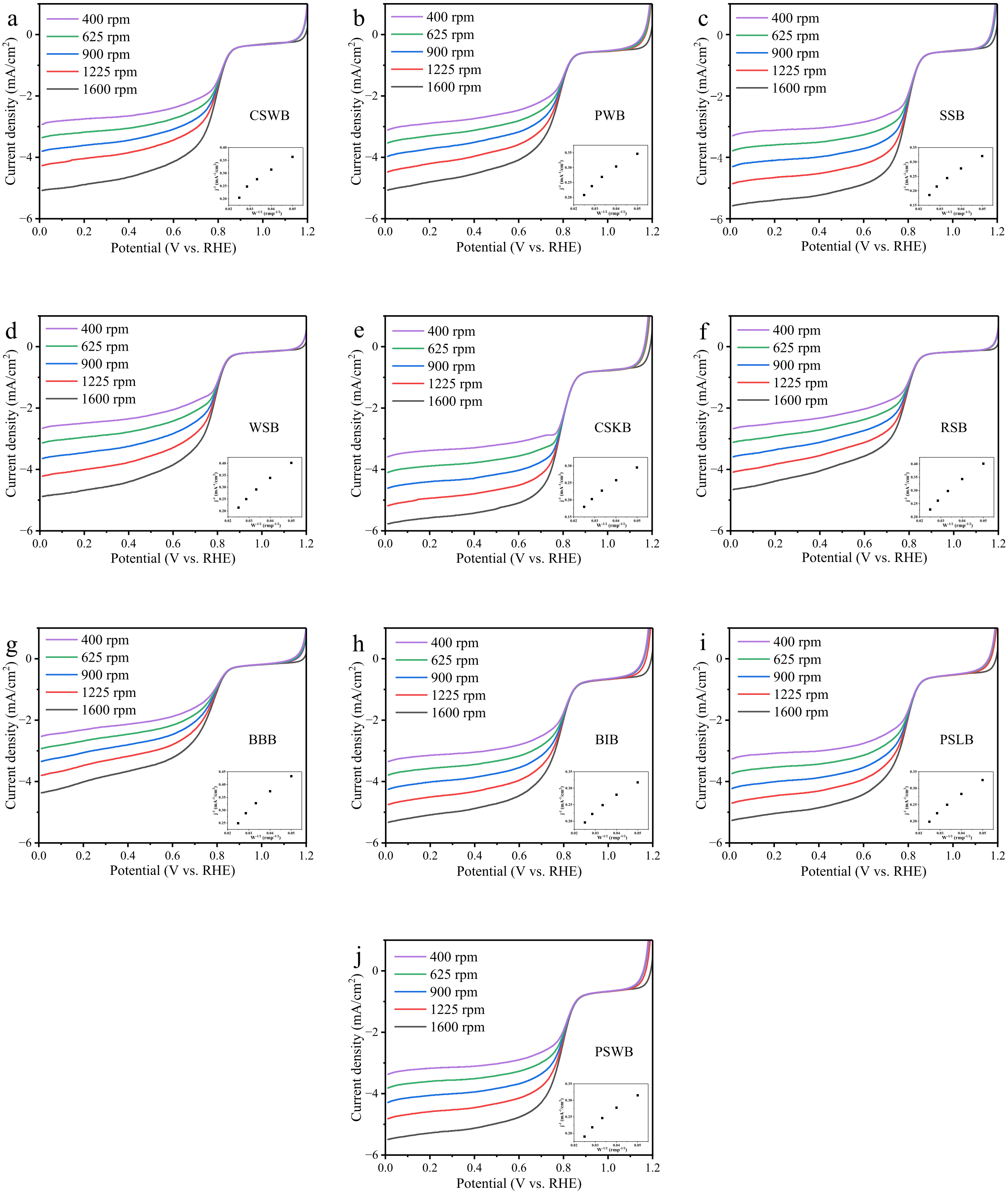

Fig. 13. Rotating disk electrode (RDE) linear sweep voltammetry (LSV) curves of the porous N-doped biochar for ORR at various rotation speeds.

the slopes of the other samples all fell within the higher range of 110–147 mV/dec, corresponding to relatively slow ORR kinetics, mainly limited by lower S_{BET} and active site density. This suggested that the Tafel slope alone cannot fully determine the overall catalytic performance of ORR catalysts. A comprehensive evaluation must include other factors such as surface area, porosity, and active site availability.

Catalytic efficiency was further gauged by deriving the electrochemical surface area (ECSA) via the double-layer capacitance, which was obtained via CV tests at 2–10 mV/s within the non-Faradaic region. The results are placed in Fig. 15(c) and (d). CSKB displayed the highest double-layer capacitance (54.34 mF/cm^2), significantly higher than the values obtained for the other samples (ranging from 39.46 to 53.73 mF/

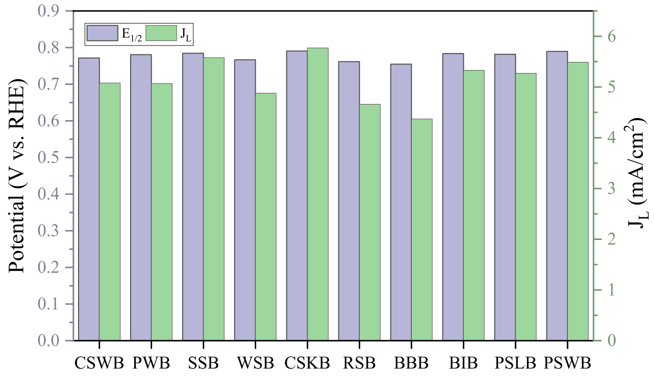

Fig. 14. The $E_{1/2}$ and J_L at 1600 rpm of porous N-doped biochar.

cm^2. Since double-layer capacitance is positively correlated with ECSA, these findings suggested that CSKB had a significantly larger electrochemically active surface area. The combination of high ECSA and optimized pore architecture provided more accessible active sites and a reaction interface for O_2 adsorption and electron transfer, explaining the superior ORR electrocatalytic performance observed in CSKB.

To further investigate the charge transfer capability and interfacial resistance of the porous N-doped biochar during the ORR tests. The Nyquist plots are shown in Fig. 16. The EIS data were fitted using ZView software, and the inset presents the equivalent circuit used for fitting. The equivalent circuit consists of R_s, R_{ct}, double-layer capacitance, and Warburg elements, which can simultaneously describe electronic conduction and interface behavior. In the Nyquist plots, the diameter of the high-frequency semicircle is R_{ct}, reflecting the speed of interface electron transfer; the low-frequency straight line corresponds to diffusion

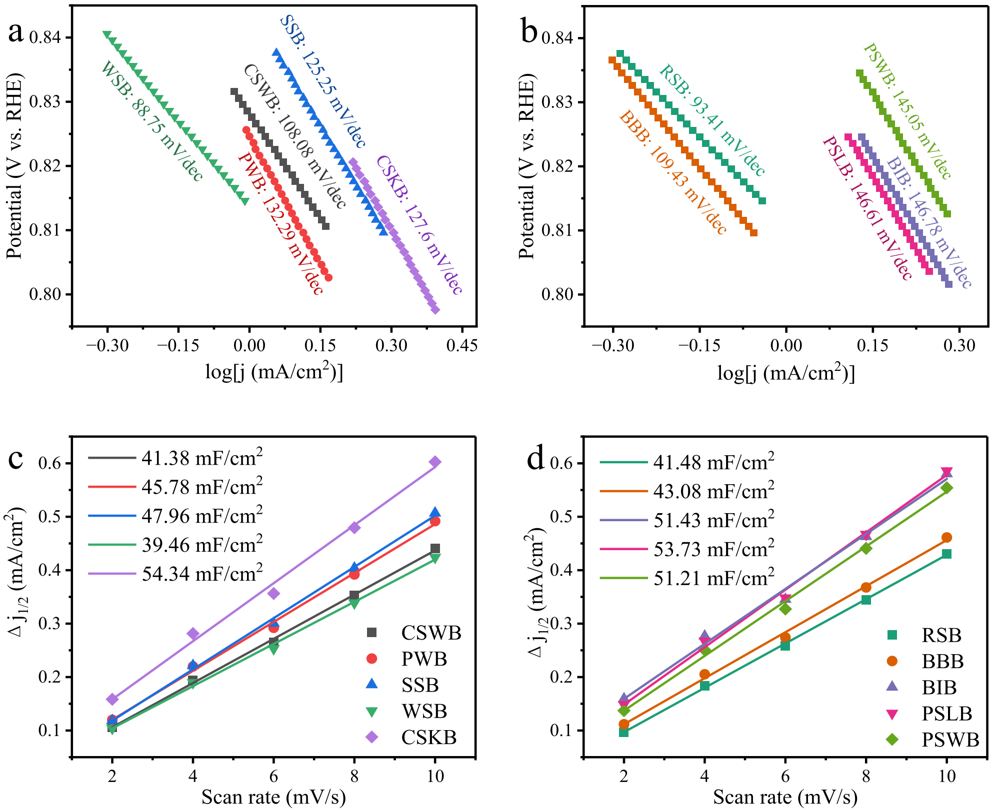

Fig. 15. The Tafel curves (a and b) and double-layer capacitance tests (c and d) of porous N-doped biochar.

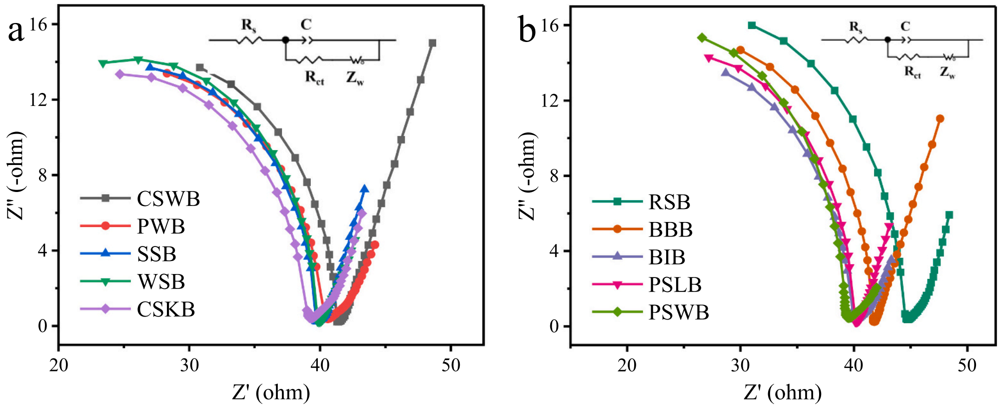

Fig. 16. The Nyquist plots of porous N-doped biochar (Illustration: Equivalent circuit diagram).

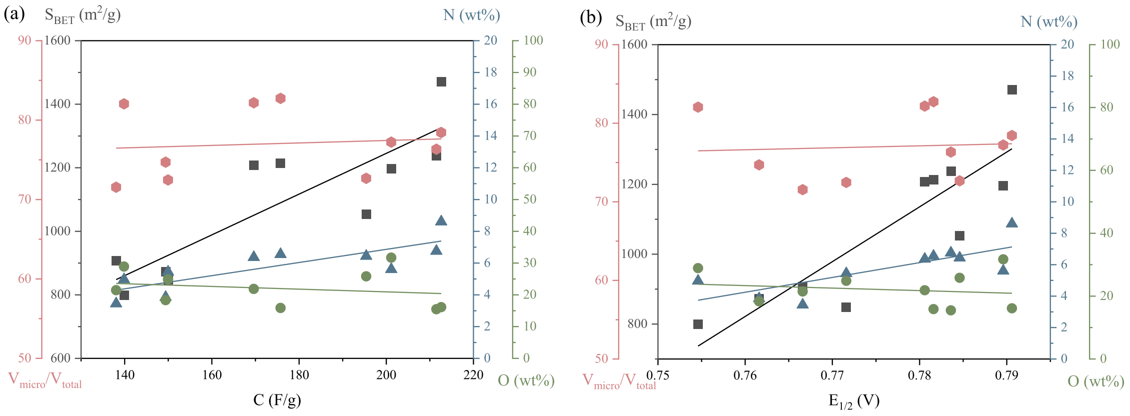

Fig. 17. The relationship between the specific capacitance (a), $E_{1/2}$ (b) and the characteristics of the N-doped biochar.

control; the curve and the intercept of the real axis are R_s, covering the electrolyte, electrode intrinsic, and contact resistance. Based on the fitting results, the CSKB exhibited the lowest R_{ct} and R_s values, calculated to be 27.43 Ω and 8.55 Ω, respectively. The small R_{ct} indicated that CSKB facilitates faster electron transfer during the ORR process, while the low Rs reflected its excellent overall electrical conductivity and favorable electrode-electrolyte interface contact. Overall, the excellent EIS performance of CSKB further confirmed its structure-performance advantages in ORR catalysis, consistent with the trends observed in CV, LSV, and Tafel analyses. The results indicated biomass-derived, porous N-doped biochar as an encouraging, low-cost catalyst for green energy equipment, including fuel cells and metal-air batteries.

To further explore the relationship among structure characteristics of porous N-doped biochar and their electrochemical performance, the correlations among specific capacitance (F/g), half-wave potential ($E_{1/2}$), and structural parameters are shown in Fig. 17. Specifically, the specific capacitance and $E_{1/2}$ at 0.5 A/g were plotted against the S_{BET}, V_{micro}/V_{total}, and N content S_{BET}, V_{micro}/V_{total}, and N content. This was because a large surface area provides more space for charge storage, while higher N content introduced pseudo-capacitance, improved electrolyte wettability, and facilitated charge accumulation. Although studies have reported the effective generation of pseudo-capacitance effects (Lin et al., 2022), O content exhibited a certain degree of negative correlation. On one hand, its contribution to capacitance was relatively weaker compared to N content. On the other hand, the loading of nitrogen content in this study competed with the retention of oxygen, limiting its effectiveness to some extent. While micropores effectively enhance the surface area, excessive micropore content may lead to prolonged ion diffusion paths during electrochemical processes. This results in increased ion transport resistance and hinders efficient charge storage and release (Yakaboylu et al., 2021). A rational pore size distribution is critical for achieving both high capacitance and rapid ion transport kinetics. It also indicated that there existed a complex synergistic among surface area, microporosity, and N content in determining the electrochemical behavior of biochar.

Besides, $E_{1/2}$ also increased with the increase of S_{BET}, V_{micro}/V_{total}, and N content. Quaternary-N and pyridinic-N are the primary contributors to ORR active sites (Li et al., 2016), which could introduce additional electrons and create catalytically active sites (Matter et al., 2006). Pyrrolic-N can also influence ORR performance by altering the electronic properties of the biochar. There may be a synergistic effect between pyrrolic-N, pyridinic-N, and quaternary-N, collectively enhancing ORR activity (Du et al., 2015). A high S_{BET} combined with a well-developed hierarchical porous structure facilitates efficient contact between the electrolyte and active sites, ensuring effective mass transport. The PSLB and PWB samples exhibit abnormal behavior, with V_{micro}/V_{total} for $E_{1/2}$ exceeding the fitted values. This indicated that further increases in micropore volume did not result in higher $E_{1/2}$ values. This may stem from limited ion accessibility within the active biochar micropores, likely due to prolonged ion entry times into the electrode micropores. Mesoporous structures can enhance ion accessibility within the pores (Dehkhoda et al., 2016). Micropores enlarge the surface and host the majority of active sites, mesopores act as rapid ion channel that cut diffusion resistance, and macropores shorten mass-transfer paths by buffering reactant and electrolyte supply (Zaman et al., 2021). In summary, porous N-doped biochar with high S_{BET}, N content, and a well-optimized micropore-to-total pore volume ratio exhibited superior performance in both supercapacitor and ORR applications.

As distinct, CSKB delivers a higher capacitive performance of 212.6 F/g and ORR performance $E_{1/2}$ of 0.791 V. The electrochemical performance of the CSKB was compared to that of other materials in Table S1 and S2. Although the primary objective of this study was to perform a correlation analysis, the electrochemical performance of CSKB exhibited relatively above-average level and can be applied as a promising industrial approach to produce electrode materials for the applications of supercapacitors and catalysts.

4. Conclusion

This study systematically investigated synchronous pyrolysis-activation-ammoniation of biomass for N-doped biochar and its electrochemical applications, and constructed the relationship between biomass, biochar, and electrochemical performance. The results demonstrated that ammonia significantly enhanced the N content of the biochar, with the cotton stalk biochar reaching 8.61 wt%. Meanwhile, the oxygen content was substantially reduced. KOH activation promoted the development of porous structures, achieving a maximum S_{BET} of 1470.99 m^2/g for CSKB. Quantitative results of XPS show that pyridine-N, pyrrole-N and quaternary-N are the primary N-containing functional groups in CSKB, with the absolute content accounting for 2.8 at%, respectively, serving as the primary source of ORR active sites; oxygen functional groups are primarily O-C═O/C-O and O-C═O/-OH, whose surface concentration not only improves electrolyte wetting but also synergistically provides additional pseudo-capacitance with pyridine-N. CSKB exhibited a specific capacitance of 212.6 F/g at 0.5 A/g, retaining 84 % of its capacity at 10 A/g. In ORR performance evaluation, CSKB achieved a $E_{1/2}$ of 0.791 V and a J_L of 5.77 mA/cm^2, along with the lowest R_{ct} (0.79 Ω) and R_s (0.006 Ω) values. In summary, Biomass with high lignin content and low ash content is most conducive to the preparation of porous N-doped carbon with high S_{BET}, high N content, and rich in pyridine-N, pyrrole-N, quaternary-N and O-C═O/-OH and O-C═O/C═O functional groups; These structures collectively contribute to high specific capacitance and excellent ORR activity. Cellulose and hemicellulose showed a slight negative correlation with S_{BET} and N content, as their decomposition during pyrolysis contributed less to carbon retention and pore development. This work clarified the preparation of porous N-doped biochar and reveals the significant relationship among biomass properties, biochar properties, and electrochemical performance. The findings provided both theoretical insights and practical guidance to utilize the full potential of varied biomass feedstocks and the green preparation of multifunctional biochar for renewable energy applications.

CRediT authorship contribution statement

Xuan Tao: Writing – review & editing, Writing – original draft, Visualization, Validation, Supervision, Methodology, Formal analysis. **Xu Chen:** Writing – review & editing, Supervision, Resources, Project administration, Investigation, Funding acquisition, Formal analysis, Conceptualization. **Zhen Fang:** Resources, Project administration, Methodology, Conceptualization. **Wei Chen:** Writing – review & editing, Supervision, Resources, Project administration, Methodology, Investigation, Funding acquisition, Conceptualization. **Zijun Pan:** Writing – review & editing, Validation, Supervision, Investigation. **Xiaolei Shi:** Supervision, Project administration, Investigation, Conceptualization. **Yurou Wang:** Writing – original draft, Visualization, Validation, Supervision, Software, Methodology, Formal analysis, Data curation.

Declaration of Competing interest

The authors declare that they have no known competing financial interests or personal relationships that could have appeared to influence the work reported in this paper.

Acknowledgment

We express great appreciation for the financial support from the National Natural Science Foundation of China (52106243, 52125601, 52376196), Natural Science Foundation of Jiangsu Province (BK20221517, BK20231477, BK20231003), and China Postdoctoral Science Foundation (2023M731715, 2025T180157), Jiangsu Shuangchuang Talent Program (JSSCBS20220359, JSSCBS20230078).

Appendix A. Supporting information

Supplementary data associated with this article can be found in the online version at doi:10.1016/j.indcrop.2025.122284.

Data availability

Data will be made available on request.

References

de Almeida, L.S., Oreste, E.Q., Maciel, J.V., Heinemann, M.G., Dias, D., 2020. Electrochemical devices obtained from biochar: advances in renewable and environmentally-friendly technologies applied to analytical chemistry. Trends Environ. Anal. Chem. 26, e00089. https://doi.org/10.1016/j.teac.2020.e00089.

Arkhipova, E.A., Novotortsev, R.Y., Ivanov, A.S., Maslakov, K.I., Savilov, S.V., 2022. Rice husk-derived activated carbon electrode in redox-active electrolyte - new approach for enhancing supercapacitor performance. J. Energy Storage 55, 105699. https://doi.org/10.1016/j.est.2022.105699.

Chen, W., Fang, Y., Li, K., Chen, Z., Xia, M., Gong, M., Chen, Y., Yang, H., Tu, X., Chen, H., 2020a. Bamboo wastes catalytic pyrolysis with N-doped biochar catalyst for phenols products. Appl. Energy 260, 114242. https://doi.org/10.1016/j.apenergy.2019.114242.

Chen, W., Gong, M., Li, K., Xia, M., Chen, Z., Xiao, H., Fang, Y., Chen, Y., Yang, H., Chen, H., 2020b. Insight into KOH activation mechanism during biomass pyrolysis: chemical reactions between O-containing groups and KOH. Appl. Energy 278, 115730. https://doi.org/10.1016/j.apenergy.2020.115730.

Chen, W., Li, K., Xia, M., Yang, H., Chen, Y., Chen, X., Che, Q., Chen, H., 2018. Catalytic deoxygenation co-pyrolysis of bamboo wastes and microalgae with biochar catalyst. ENERGY 157, 472–482. https://doi.org/10.1016/j.energy.2018.05.149.

Chen, W., Tao, X., Shi, X., Guo, W., Wang, Y., Liu, B., Yang, H., 2024. Insight into catalytic effects of alkali metal salts addition on bamboo and cellulose pyrolysis. npj Mater. Sustain. 2, 25. https://doi.org/10.1038/s44296-024-00028-6.

Chen, Y., Zhang, X., Chen, W., Yang, H., Chen, H., 2017. The structure evolution of biochar from biomass pyrolysis and its correlation with gas pollutant adsorption performance. Bioresour. Technol. 246, 101–109. https://doi.org/10.1016/j.biortech.2017.08.138.

Culaba, A.B., Mayol, A.P., Bandala, A.A., Ii, R.S.C., Alipio, M., Chen, W.-H., Show, P.L., Chang, J.-S., Juan, J.L.G.S., Ubando, A.T., 2023. Design of biorefineries towards carbon neutrality: a critical review. Bioresour. Technol. 369, 128256. https://doi.org/10.1016/j.biortech.2022.128256.

Dehkhoda, A.M., Gyenge, E., Ellis, N., 2016. A novel method to tailor the porous structure of KOH-activated biochar and its application in capacitive deionization and energy storage. Biomass. Bioenerg. 87, 107–121. https://doi.org/10.1016/j.biombioe.2016.02.023.

Ding, X.-B., Li, F., Cao, Q.-C., Wu, H., Qin, Y.-H., Li, Y., Wang, T., Zheng, X., Wang, C.-W., 2022. Core-shell S-doped g-C_3N_4@P123 derived N and S co-doped carbon as metal-free electrocatalysts highly efficient for oxygen reduction reaction. Chem. Eng. J. 429. https://doi.org/10.1016/j.cej.2021.132469.

Du, R., Zhang, N., Zhu, J., Wang, Y., Xu, C., Hu, Y., Mao, N., Xu, H., Duan, W., Zhuang, L., Qu, L., Hou, Y., Zhang, J., 2015. Nitrogen-doped carbon nanotube aerogels for high-performance ORR catalysts. Small 11, 3903–3908. https://doi.org/10.1002/smll.201500587.

Duan, X., Wang, J., Zhao, Z., Zhao, H., Cheng, M., Wang, C., Lei, Y., Wang, J., Wang, J., 2019. Poly-melamine sponge derived N-doped carbon/Fe_3O_4/graphene synthesized for lithium-ion anode. Mater. Lett. 251, 57–60. https://doi.org/10.1016/j.matlet.2019.05.035.

Fu, S., Li, M., de Jong, W., Kortlever, R., 2023. Tuning the properties of n-doped biochar for selective CO_2 electroreduction to CO. ACS Catal. 13, 10309–10323. https://doi.org/10.1021/acscatal.3c01773.

Grafmüller, J., Böhm, A., Zhuang, Y.L., Spahr, S., Müller, P., Otto, T.N., Bucheli, T.D., Leifeld, J., Giger, R., Tobler, M., Schmidt, H.P., Dahmen, N., Hagemann, N., 2022. Wood ash as an additive in biomass pyrolysis: effects on biochar yield, properties, and agricultural performance. ACS Sustain. Chem. Eng. 10, 2720–2729. https://doi.org/10.1021/acssuschemeng.1c07694.

He, J.K., Zhao, Y.Y., Zhou, Y., Wu, S.B., 2023. Preparation of high-performance activated carbons from hemicellulose pre-extracted residues of poplar and their application in VOCs removal. Bioresources 18, 2874–2896. https://doi.org/10.15376/biores.18.2.2874-2896.

Larter, N.C., 1992. Forage fiber analyses - a comparison of 2 techniques. Wildl. Res. 19, 289–293. https://doi.org/10.1071/wr9920289.

Li, Y.-h, Chang, F.-m, Huang, B., Song, Y.-p, Zhao, H.-y, Wang, K.-j, 2020. Activated carbon preparation from pyrolysis char of sewage sludge and its adsorption performance for organic compounds in sewage. FUEL 266, 117053. https://doi.org/10.1016/j.fuel.2020.117053.

Li, J.-C., Hou, P.-X., Zhao, S.-Y., Liu, C., Tang, D.-M., Cheng, M., Zhang, F., Cheng, H.-M., 2016. A 3D bi-functional porous N-doped carbon microtube sponge electrocatalyst for oxygen reduction and oxygen evolution reactions. Energy Environ. Sci. 9, 3079–3084. https://doi.org/10.1039/c6ee02169g.

Li, J., Lv, F., Yang, R., Zhang, L., Tao, W., Liu, G., Gao, H., Guan, Y., 2022. N-doped biochar from lignocellulosic biomass for preparation of adsorbent: characterization, kinetics and application. Polymers 14 (18), 3889. https://doi.org/10.3390/polym14183889.

Li, Z., Zhang, L., Amirkhiz, B.S., Tan, X.H., Xu, Z.W., Wang, H.L., Olsen, B.C., Holt, C.M.B., Mitlin, D., 2012. Carbonized chicken eggshell membranes with 3D architectures as high-performance electrode materials for supercapacitors. Adv. Energy Mater. 2, 431–437. https://doi.org/10.1002/aenm.201100548.

Lian, F., Cui, G., Liu, Z., Duo, L., Zhang, G., Xing, B., 2016. One-step synthesis of a novel N-doped microporous biochar derived from crop straws with high dye adsorption capacity. J. Environ. Manag. 176, 61–68. https://doi.org/10.1016/j.jenvman.2016.03.043.

Lin, Y., Li, F., Zhang, Q., Liu, G., Xue, C., 2022. Controllable preparation of green biochar based high-performance supercapacitors. Ionics 28, 2525–2561. https://doi.org/10.1007/s11581-022-04557-9.

Liu, J.P., Chen, X., Chen, W., Xia, M.W., Chen, Y.Q., Chen, H.P., Zeng, K., Yang, H.P., 2023. Biomass pyrolysis mechanism for carbon-based high-value products. Proc. Combust. Inst. 39, 3157–3181. https://doi.org/10.1016/j.proci.2022.09.063.

Liu, X.R., Yang, H.P., Xue, P.X., Tang, Y.J., Ye, C., Guo, W.W., 2024. Machine learning modeling of the capacitive performance of N-doped porous biochar electrodes with experimental verification. Renew. Energy 231, 120969. https://doi.org/10.1016/j.renene.2024.120969.

Ma, H., Hansen, H.C.B., Pu, S., Ouyang, Q., Thygesen, L.G., Tobler, D.J., 2025. Nitrogen doping turns carbonaceous materials into fast-reacting catalysts for reductive dechlorination. Environ. Pollut. 368, 125578. https://doi.org/10.1016/j.envpol.2024.125578.

Matter, P.H., Zhang, L., Ozkan, U.S., 2006. The role of nanostructure in nitrogen-containing carbon catalysts for the oxygen reduction reaction. J. Catal. 239, 83–96. https://doi.org/10.1016/j.jcat.2006.01.022.

Nzediegwu, C., Arshad, M., Ulah, A., Naeth, M.A., Chang, S.X., 2021. Fuel, thermal and surface properties of microwave-pyrolyzed biochars depend on feedstock type and pyrolysis temperature. Bioresour. Technol. 320, 124282. https://doi.org/10.1016/j.actatropica.2020.124282.

Oladunni, J., Zain, J.H., Hai, A., Banat, F., Bharath, G., Alhseinat, E., 2018. A comprehensive review on recently developed carbon based nanocomposites for capacitive deionization: from theory to practice. Sep. Purif. Technol. 207, 291–320. https://doi.org/10.1016/j.seppur.2018.06.046.

Rajapaksha, A.U., Chen, S.S., Tsang, D.C.W., Zhang, M., Vithanage, M., Mandal, S., Gao, B., Bolan, N.S., Ok, Y.S., 2016. Engineered/designer biochar for contaminant removal/immobilization from soil and water: potential and implication of biochar modification. Chemosphere 148, 276–291. https://doi.org/10.1016/j.chemosphere.2016.01.043.

Rufford, T.E., Hulicova-Jurcakova, D., Zhu, Z.H., Lu, G.Q., 2009. Empirical analysis of the contributions of mesopores and micropores to the double-layer capacitance of carbons. J. Phys. Chem. C. 113, 19335–19343. https://doi.org/10.1021/jp905975q.

Song, Y., Zhang, X., Cui, X., Shi, J., 2019. The ORR kinetics of ZIF-derived Fe-N-C electrocatalysts. J. Catal. 372, 174–181. https://doi.org/10.1016/j.jcat.2019.02.023.

Sun, J., Lowe, S.E., Zhang, L., Wang, Y., Pang, K., Wang, Y., Zhong, Y., Liu, P., Zhao, K., Tang, Z., Zhao, H., 2018. Ultrathin nitrogen-doped holey carbon@Graphene bifunctional electrocatalyst for oxygen reduction and evolution reactions in alkaline and acidic media. Angew. Chem. Int. Ed. 57, 16511–16515. https://doi.org/10.1002/anie.201811573.

Sun, T., Xin-Ping, Z., Dian-Peng, L., Zhu-Yu, G., Jia-Xi, Z., Hong-Tao, J., 2017. Comparison of biochars characteristics from different raw materials. JARE 34, 543–549. https://doi.org/10.13254/j.jare.2017.0158.

Tan, Z.F., Chen, K.T., Liu, P.K., 2015. Possibilities and challenges of China's forestry biomass resource utilization. Renew. Sust. Energ. Rev. 41, 368–378. https://doi.org/10.1016/j.rser.2014.08.059.

Wan, Z., Sun, Y., Tsang, D.C.W., Khan, E., Yip, A.C.K., Ng, Y.H., Rinklebe, J., Ok, Y.S., 2020. Customised fabrication of nitrogen-doped biochar for environmental and energy applications. Chem. Eng. J. 401, 126136. https://doi.org/10.1016/j.cej.2020.126136.

Wang, Y., Guo, W., Chen, W., Xu, G., Zhu, G., Xie, G., Xu, L., Dong, C., Gao, S., Chen, Y., Yang, H., Chen, H., Fang, Z., 2024. Co-production of porous N-doped biochar and hydrogen-rich gas production from simultaneous pyrolysis-activation-nitrogen doping of biomass: Synergistic mechanism of KOH and NH 3. Renew. Energy 229, 120777. https://doi.org/10.1016/j.renene.2024.120777.

Wei, X., Jiang, X., Wei, J., Gao, S., 2016. Functional groups and pore size distribution do matter to hierarchically porous carbons as high-rate-performance supercapacitors. Chem. Mater. 28, 445–458. https://doi.org/10.1021/acs.chemmater.5b02336.

Yakaboylu, G.A., Jiang, C., Yumak, T., Zondlo, J.W., Wang, J., Sabolsky, E.M., 2021. Engineered hierarchical porous carbons for supercapacitor applications through chemical pretreatment and activation of biomass precursors. Renew. Energy 163, 276–287. https://doi.org/10.1016/j.renene.2020.08.092.

Yan, Y., Xu, M., Luo, Y., Ma, J., Pang, H., Xue, H., 2017. Preparation of N, P co-doped activated carbons derived from honeycomb as an electrode material for supercapacitors. RSC Adv. 7, 47448–47455. https://doi.org/10.1039/c7ra08759d.

Yang, Q., Zhou, H., Bartocci, P., Fantozzi, F., Masek, O., Agblevor, F.A., Wei, Z., Yang, H., Chen, H., Lu, X., Chen, G., Zheng, C., Nielsen, C.P., McElroy, M.B., 2021. Prospective contributions of biomass pyrolysis to China's 2050 carbon reduction and renewable energy goals. Nat. Commun. 12, 1698. https://doi.org/10.1038/s41467-021-21868-z.

Zaman, S., Huang, L., Douka, A.I., Yang, H., You, B., Xia, B.Y., 2021. Oxygen reduction electrocatalysts toward practical fuel cells: progress and perspectives. Angew. Chem. Int. Ed. 60, 17832–17852. https://doi.org/10.1002/anie.202016977.

Zhang, X., Cui, C., Zheng, Q., Wang, Y., Chang, J., Wang, S., 2021. Development of highly efficient and reusable magnetic nitrogen-doped carbon nanotubes for chlorophenol removal. Environ. Sci. Pollut. Res. 28, 37424–37434. https://doi.org/10.1007/s11356-021-13302-0.

Zhang, P., Duan, W., Peng, H., Pan, B., Xing, B., 2022. Functional Biochar and Its Balanced Design. ACS Environ. Au 2, 115–127. https://doi.org/10.1021/acsenvironau.1c00032.

Zhang, C., Song, W., Ma, Q., Xie, L., Zhang, X., Guo, H., 2016. Enhancement of CO_2 capture on biomass-based carbon from black locust by KOH activation and ammonia modification. Energ Fuel 30, 4181–4190. https://doi.org/10.1021/acs.energyfuels.5b02764.

Zhang, D., Zhang, Y., Liu, H., Xu, Y., Wu, J., Li, P., 2023. Effect of pyrolysis temperature on carbon materials derived from reed residue waste biomass for use in supercapacitor electrodes. J. Phys. Chem. Solids 178, 111318. https://doi.org/10.1016/j.jpcs.2023.111318.

Zhang, X., Zhang, S., Yang, H., Feng, Y., Chen, Y., Wang, X., Chen, H., 2014. Nitrogen enriched biochar modified by high temperature CO_2-ammonia treatment: characterization and adsorption of CO_2. Chem. Eng. J. 257, 20–27. https://doi.org/10.1016/j.cej.2014.07.024.

Zhao, C., Ge, L.C., Wang, R.K., Chu, H.Q., Mai, L.H., Zha, W.T., Wang, Y., Xu, C., 2023. Effects of cellulose addition on the physicochemical properties, pore structure and iodine adsorption of lignin-based biochar. Fuel 352, 9. https://doi.org/10.1016/j.fuel.2023.129061.

Zhu, S., Huang, X., Ma, F., Wang, L., Duan, X., Wang, S., 2018. Catalytic removal of aqueous contaminants on N-doped graphitic biochars: inherent roles of adsorption and nonradical mechanisms. Environ. Sci. Technol. 52, 8649–8658. https://doi.org/10.1021/acs.est.8b01817.